ACSNANO

www.acsnano.org

ARTICLE

Bio-inspired Photonic Masquerade with Perturbative Metasurfaces

Kun Huang,* Dong Zhao, Febiana Tjiptoharsono, Yunjie Chen, Calvin Pei Yu Wong, Xiaosong Tang, Joel K. W. Yang, and Zhaogang Dong*

Cite This: *ACS Nano* 2020, 14, 7529–7537

Read Online

ACCESS | Metrics & More | Article Recommendations | Supporting Information

ABSTRACT: **Camouflage is critical for many living organisms to survive in the natural world and has stimulated applications, such as optical cloaking and military affairs. However, most applications adopt crypsis-type camouflage that prevents the organisms from being detected by matching the environment, which is challenging to realize the large angle-of-view and broadband operation at optical frequencies. Here, as inspired by nature's system of masquerade, we demonstrate an optical masquerade, being detected but not recognized, with perturbative metasurfaces that could camouflage an object into another unrelated one under the oblique (±69°) illumination of visible light with an ∼160 nm bandwidth. Predicted by the perturbation theory, the dielectric metastructures encircling a pistol-shaped object have a thin layer of nanodisk array, which can suppress the electromagnetic resonances of nanomodes for mimicking the transmitted intensity and phase of the camouflaged object. We also exhibit that optical masquerade is an invasive, environment-independent, object-unlimited, and material-extendable camouflage, which might benefit optical security, anticounterfeiting, and encoding.**

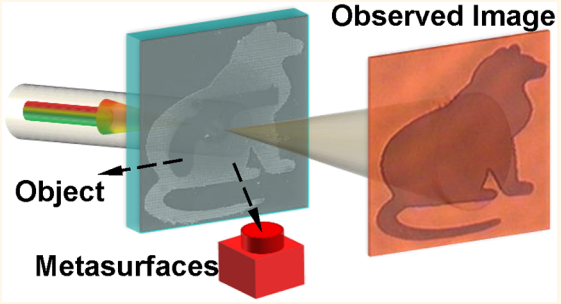

KEYWORDS: *metasurfaces, masquerade, camouflage, dielectric nanostructures, perturbation theory*

In the natural world, camouflage is an important survival technique where living organisms avoid being detected or recognized by predators or prey. Camouflaging strategies can be categorized as either crypsis or masquerade.[1] Crypsis is arguably the more familiar method in which organisms match their physical properties (*e.g.*, color, lightness, transparency, reflection, pattern, and shadow) to their surrounding background.[2] This crypsis-type camouflage naturally finds many applications, especially in the military with the hidden electromagnetic[3] and thermal[4,5] signatures by electromagnetic cloaking[6] with artificially structured metamaterials.[7,8] Although significant progresses have been achieved,[9−12] a perfect cloaking of objects is still challenging because it needs the aberration-free and lossless bending of broadband light at multiple angles-of-view,[13] especially at visible frequencies.[14−19]

Alternatively, some organisms masquerade themselves to avoid recognition despite being detected. Masquerading allows certain organisms such as the stick or leaf insect to mimic static or inanimate objects,[1,20] without changing their physical properties (*e.g.*, color) to blend into its surrounding. Hence, masquerade offers a low-cost approach to efficient camouflage by only slight modifications to the shape or appearance of an object, an increasing topic of interest in biology.[20] In nano-optics, the concept of masquerade can be implemented by surrounding an object with micro/nanostructures, so that their combined pattern is misidentified as another unrelated object. With masquerade, optical camouflage is simplified to match the optical properties of the object with its surrounding micro/nanostructures, instead of to an arbitrary background. For example, optical metasurfaces,[21−38] composed of two-dimensional spatially varying nanostructures, are suitable for matching the optical behavior of the camouflaged object because they can be designed to manipulate light in a predefined manner. Therefore, it is feasible to develop optical metasurface-based masquerade without dependence on the environment, which might suggest a promising alternative to camouflage an object robustly in addition to optical cloaking.

Here, we demonstrate an optical masquerade by camouflaging a pistol-shaped object that is surrounded by dielectric metasurfaces but is observed as a "cat" (Figure 1a). The camouflaged object is realized experimentally in a 305 nm-thick silicon (Si) film with a "pistol" pattern (Figure 1b). To

Received: April 23, 2020
Accepted: June 1, 2020
Published: June 1, 2020

https://dx.doi.org/10.1021/acsnano.0c03401
ACS Nano 2020, 14, 7529–7537

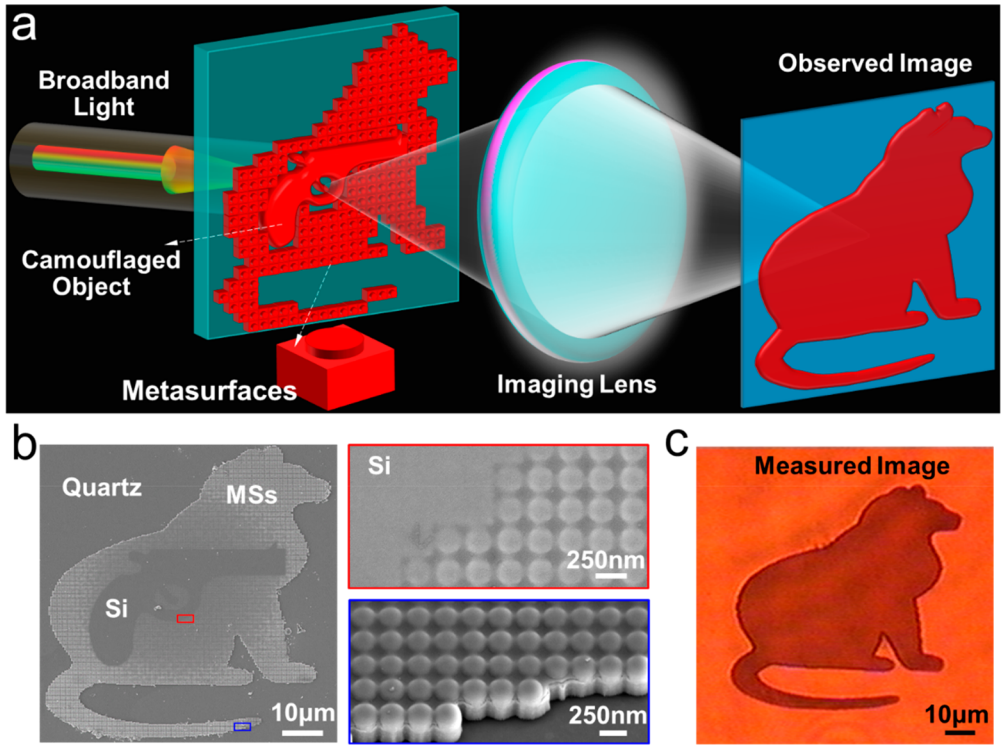

Figure 1. Optical masquerade. (a) Working principle by camouflaging a "pistol" into an unrelated "cat" with the help of metasurfaces. (b) Scanning electron micrograph (SEM) images of the fabricated sample. The upper and lower insets in the right panels show the zoomed-in image of the samples located in the red and blue rectangles of the left panel. (c) Transmission microscopy image of the sample under the illumination of a broadband laser.

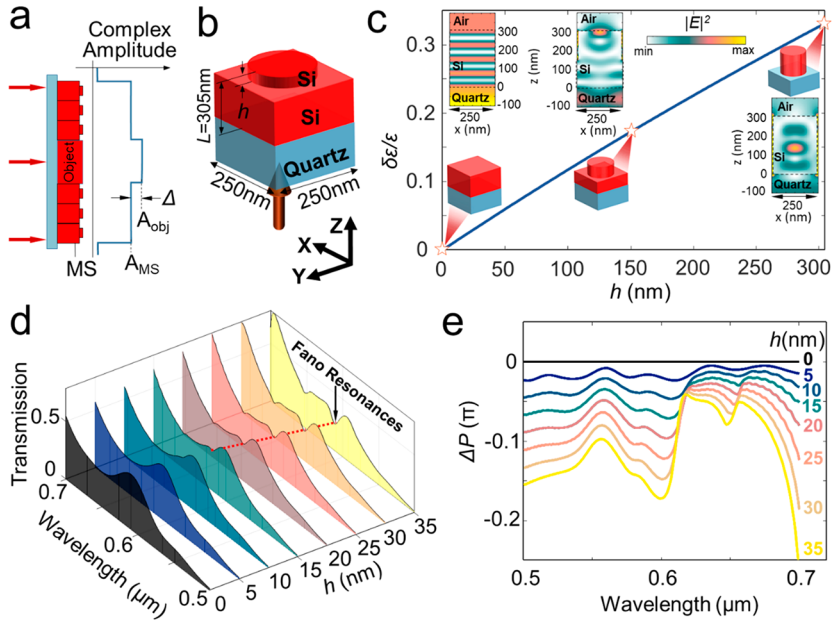

Figure 2. Design of perturbative metasurfaces. (a) Sketch describing the optical responses of the object and metasurfaces (MS). The difference Δ between their transmitted complex amplitudes should be minimized to realize the masquerade. (b) A 250 nm × 250 nm unit cell of the proposed metasurfaces with an *h*-thick nanodisk array. (c) The changed permittivity (normalized to the permittivity of the material Si) for different *h* values. The insets show the electric fields within the metastructures for *h* = 0, 150, and 305 nm, revealing the appearance of electromagnetic nanomodes. (d) Simulated transmission of the metastructure with its *h* ranging from 0 to 35 nm with an interval of 5 nm. The valley labeled by the red-dashed line indicates the generation of nanomodes. (e) Simulated phase difference Δ*P* (= *P*(*h*) − *P*(0)) of a metastructure with different *h* values.

masquerade it, a perturbative layer induced by a 15 nm-thick nanodisk array located on a 290-thick Si film is employed in the dielectric metasurfaces to mimic optical transmission of the object "pistol". When illuminated by a broadband white-light laser, the fabricated sample shows a transmitted pattern of only a "cat" (Figure 1c). It indicates an efficient camouflage because

https://dx.doi.org/10.1021/acsnano.0c03401
ACS Nano 2020, 14, 7529−7537

the object "pistol" is invisible at a large angle-of-view of ~138° in the experiment.

RESULTS AND DISCUSSION

Design of Perturbative Metasurfaces. To realize such an optical masquerade, the difference between the complex amplitudes (*i.e.*, A_{MS} and A_{obj} in Figure 2a) of light transmitted from the metasurfaces and the object is minimized within a wide spectrum. In this work, the camouflaged object is made of a thin film, which has the wavelength-dependent transmission dominated by only FP resonance (related with longitudinal modes) of the plane wave. Therefore, we propose a metastructure containing a top layer (with a thickness of h) of a nanodisk array and a bottom Si film (Figure 2b). The top-layer nanodisk array is introduced to manipulate the transverse modes that are related with Mie resonances while the bottom Si film is used to maintain the required FP resonances. The fraction of Mie and FP resonances can be tuned after a careful design of the metastructure, so that the resulting optical response approaches that of the object film.

The metastructure becomes a pure film (*i.e.*, the object) of 305 nm thickness for h = 0 nm but is shaped into the commonly used nanodisk metasurfaces for $h = L$ (the thickness L of object film is 305 nm). When h is small, the top nanodisk array could be taken as a perturbative item in the metastructure. According to the perturbation theory,[39] when an electromagnetic wave passes through the metastructures, its electric displacement $\mathbf{D}$ could be described by

$$\mathbf{D} = \mathbf{D}^{(0)} + \frac{1}{4\pi}\int \frac{e^{ik|\mathbf{x}-\mathbf{x}'|}}{|\mathbf{x}-\mathbf{x}'|}[\nabla' \times \nabla' \times (\mathbf{D} - \varepsilon\mathbf{E}) + i\varepsilon\omega\nabla' \times (\mathbf{B} - \mu\mathbf{H})]\, d^3\mathbf{x}' \quad (1)$$

where $\mathbf{D}^{(0)}$ is the electric displacement for the case h = 0 without any perturbation, $\mathbf{E}$ and $\mathbf{H}$ are the electric and magnetic fields, $\mathbf{B}$ is the magnetic induction, ε and μ are the electric permittivity and magnetic permeability of the film, k and ω are the wavenumber and frequency of the incident wave, and $\mathbf{x}'$ and $\mathbf{x}$ are the spatial coordinates of the metastructure and the position of interest, respectively.

Since the perturbation item exists in the metastructure, $\mathbf{D}$ and $\mathbf{B}$ are slightly deviated from $\varepsilon\mathbf{E}$ and $\mu\mathbf{H}$, respectively. By using the first Born approximation,[39] we have $\mathbf{D} = (\varepsilon + \delta\varepsilon)\mathbf{E}$ and $\mathbf{B} = (\mu + \delta\mu)\mathbf{H}$, where $\delta\varepsilon$ and $\delta\mu$ are the changed permittivity and permeability. Considering that no magnetic material is involved here, we have $\delta\mu = 0$ so that the contribution from the magnetic part could be ignored in eq 1. Thus, the difference between $\mathbf{D}$ and $\mathbf{D}^{(0)}$ is expressed as

$$\delta\mathbf{D} = \mathbf{D} - \mathbf{D}^{(0)} \approx \frac{1}{4\pi}\int \frac{e^{ik|\mathbf{x}-\mathbf{x}'|}}{|\mathbf{x}-\mathbf{x}'|}[\nabla' \times \nabla' \times (\delta\varepsilon\cdot\mathbf{E})]\, d^3\mathbf{x}' \quad (2)$$

Because $\mathbf{D}$ and $\mathbf{D}^{(0)}$ are related to the optical behavior of the metastructure and the object, respectively, $\delta\mathbf{D}$ is a good parameter to evaluate the masquerade indirectly. Equation 2 indicates that a small $\delta\varepsilon$ results in a small $\delta\mathbf{D}$, which is preferred for the purpose of masquerade.

Theoretically, the changed permittivity can be calculated by using $\delta\varepsilon = \varepsilon - \varepsilon_{eff}$, where ε_{eff} is the effective permittivity of the metastructure. Since the metastructure has the subwavelength period at the transverse plane (*i.e.*, x–y) and a small h along the longitudinal direction (*i.e.*, z), its effective permittivity can be approximated by the Maxwell-Garnett formula[40] $\frac{\varepsilon_{eff} - \varepsilon}{\varepsilon_{eff} + 2\varepsilon} = f\frac{\varepsilon_{air} - \varepsilon}{\varepsilon_{air} + 2\varepsilon}$, where ε_{air} and f are the permittivity and volume fraction of the air surrounding the nanodisks, respectively. After a simple mathematical operation, we have $\frac{\delta\varepsilon}{\varepsilon} = \left[\left(\frac{\varepsilon}{\varepsilon - \varepsilon_{air}} - \frac{1}{3}\right)\frac{1}{f} + \frac{1}{3}\right]^{-1}$. In our case, when the periodic metastructures with small pixel pitches are considered, the air surrounding the nanodisk array can be taken to be quasi-uniform over the entire metadevice. Thus, its volume fraction can be approximated by $f \approx h(p^2 - \pi r^2)/(Lp^2)$, where p is the transverse period of metastructure, L is the total thickness, and r is the radius of the nanodisk. After substituting $\delta\varepsilon$ into eq 2, we eventually arrive at

$$\delta\mathbf{D} \approx \frac{1}{4\pi}\int \frac{e^{ik|\mathbf{x}-\mathbf{x}'|}}{|\mathbf{x}-\mathbf{x}'|}\nabla' \times \nabla' \times \left(\frac{\varepsilon}{\left(\frac{\varepsilon}{\varepsilon - \varepsilon_{air}} - \frac{1}{3}\right)\frac{Lp^2}{h(p^2 - \pi r^2)} + \frac{1}{3}}\cdot\mathbf{E}\right) d^3\mathbf{x}' \quad (3)$$

where $\delta\mathbf{D}$ connects with the geometry (*i.e.*, L, h, r, and p) of the metastructure. Equation 3 is valid for small h and p because the effective permittivity is derived under the approximation that the air is uniformly distributed. Thus, one unit of metastructure is approximated as a homogeneous unit with the permittivity ε_{eff}, which implies that the nanomodes induced by the h-thick nanodisks are ignored.

Equation 3 is instructive to design the metastructure for optical masquerade. If the total thickness L and the period p of the metastructure are given in this work, eq 3 suggests an efficient masquerade (*i.e.*, a small $\delta\mathbf{D}$) by decreasing h and increasing r. On the basis of this result, the diameter ($2r$) of the nanodisk is chosen to be as large as 240 nm, which approaches the period of p = 250 nm in our metastructure. Figure 2c shows that, with the increment of h, the transverse nanomodes become gradually dominated in the metastructure, accompanying the disappearance of plane wave-based FP resonances and the increased $\delta\varepsilon$. For the case $h = L$, the metastructure becomes a traditional metasurface that supports the nanomode-based FP resonances, which however, have a different response from the plane wave-based FP resonances. Therefore, we infer that a maximum h_{max} must exist so that the metastructure with $0 < h \le h_{max}$ behaves like the object.

To determine h_{max}, a rigorous numerical simulation is implemented by using a finite-difference time-domain (FDTD) method within a pixel pitch of 250 nm × 250 nm, where the periodic boundaries are employed along the x and y directions and the perfect-matching layers are applied in the z direction. The experimentally measured refractive index (see Figure S1) of Si is adopted in our FDTD model to avoid the discrepancy between the simulated and experimental results. Figure 2d shows the simulated transmission over the spectrum from 500 to 700 nm at different h values. It reveals that the nanomodes confined in the nanodisk array appear when h > 15 nm, so that the destructive interference between the radiation of these nanomodes and the background light leads to the valleys of transmission spectrum (Fano resonances[41]) labeled by the red-dashed line. Near the resonating wavelength, the phase of transmitted light has a rapid variation (see Figure 2e), which indicates a delay between the driving source and the response

https://dx.doi.org/10.1021/acsnano.0c03401
ACS Nano 2020, 14, 7529–7537

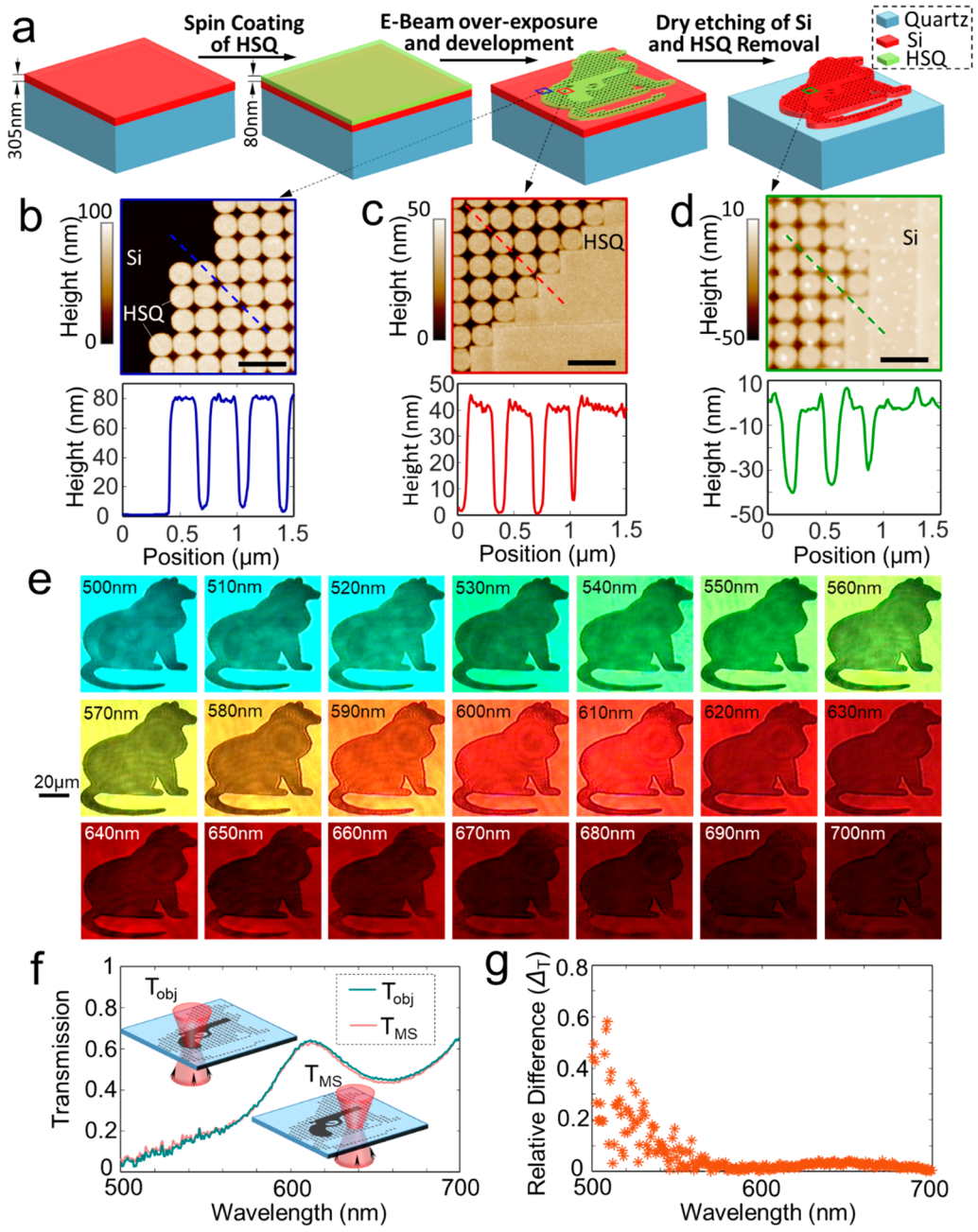

Figure 3. Experimental demonstration of the optical masquerade. (a) Flow of fabrication processes by using E-beam lithography. HSQ: hydrogen silsesquioxane (HSQ) resist. (b, c) Atomic force microscopy (AFM) images of the photoresist after development. The outmost (b) and inner (c) images show the different depths of the photoresist due to the different scattering of the electrons. The relative line-scanning profiles are shown below the AFM images. (d) AFM picture of the final sample after dry etching and HSQ removal. The line-scanning profile shown below indicates that the depth of the silicon nanodisk is around 30 nm. Scale bars: 500 nm. (e) Measured microscopic images of the fabricated sample illuminated by the laser with the wavelengths from 500 to 700 nm. (f) Experimental transmission spectra of object (T_{obj}) and metastructures (T_{MS}). The insets show the ways of characterizing T_{obj} and T_{MS}. (g) Relative difference ΔT of the measured transmission.

of the oscillator.[42] It leads to the enhanced phase modulation, which is not desired here. Meanwhile, when h increases, the phase difference between the corresponding metastructure and the object film (h = 0) enlarges quickly due to the coexistence of the phase accumulation and the resonances of nanomodes.

Considering that the nanomodes reshape the optical response of the metastructure in an undesired way, we employ h = 15 nm in this work to avoid the excitation of the confined nanomodes. Thus, our metastructure with h = 15 nm presents the perturbative metasurfaces that can mimic the camouflaged object with a trivial difference in the transmission (<0.12, Figure 2d) and phase (<0.08π, Figure 2e). In one unit of the metastructure with h = 15 nm, the simulated electric fields at the typical wavelengths of 500, 600, and 700 nm are shown in Figure S2, which doubly confirms the good match between the optical responses of the metastructure and the object.

EXPERIMENTAL DEMONSTRATION

We fabricate the exemplified samples on the 305 nm-thick Si film by using the E-beam lithography (ELS-7000, Elionix) with an overexposed dosage, resulting in a 3-dimensional photo-

https://dx.doi.org/10.1021/acsnano.0c03401
ACS Nano 2020, 14, 7529−7537

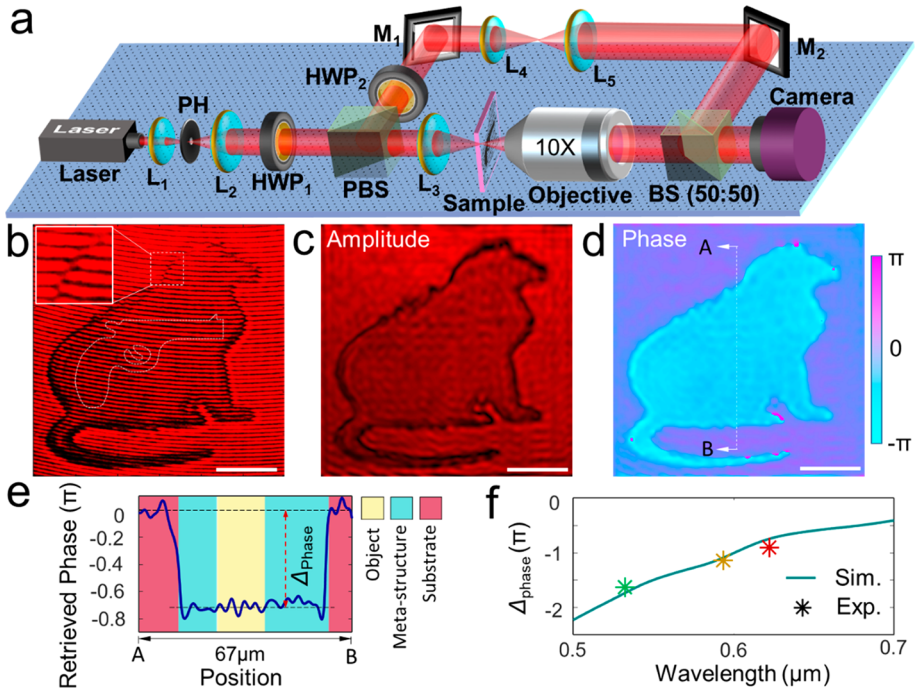

Figure 4. Phase measurement. (a) Sketch of the experimental setup for characterizing the phase in a Mach−Zehnder interferometer. L: lens; HWP: half-wave plate; M: mirror; BS: beam splitter; PBS: polarization beam splitter; PH: pinhole. (b) Recorded interference pattern at the wavelength of 633 nm. The inset is a zoomed-in image across the boundary between the metastructures and substrate, where the dislocation of the fringes indicates the phase difference. Scale bar: 20 μm. (c, d) Retrieved amplitude (c) and phase (d) from the experimental interference pattern. Scale bar: 20 μm. (e) Line-scanning intensity of the retrieved phase along AB in (d). The regions of the object, metastructures, and substrate are labeled in different colors. (f) Phase difference Δ_{phase} between the substrate and the "cat" pattern. The simulated Δ_{phase} is calculated as the difference between the phase delay caused by the metastructures and substrate, where the calculation of phase delay is numerically implemented by using FDTD. The experimental Δ_{phase} is extracted from the retrieved phase (as shown in (e)) at the wavelengths of 532, 593, and 633 nm.

resist pattern (see Figure 3a) due to the strong backscattering of electrons. To check its profile of photoresist after development, atomic force microscopy (AFM) with a high-aspect-ratio probe (Bruker TESP-HAR) of 10 nm in radius is employed, yielding the 3-dimensional profiles at both outmost (Figure 3b) and inner (Figure 3c) parts. During a dry etching process of silicon, the 3-dimensional photoresist is partially etched, thus creating the expected nanodisk array. The AFM picture (Figure 3d) of the final sample confirms the height of the silicon nanodisks to be ~30 nm, which might be caused by the residual HSQ that has little (the deviation of <2%) influence on the transmission. More details about the fabrication processes could be found in the Methods section. The scanning-electron-microscope images of our fabricated sample are shown in Figure 1b, which clearly illustrates the "pistol" pattern within the contour "cat". The achieved nanodisks have the experimental diameter of 240 nm as expected.

To characterize its performance, a self-made measuring system is built in a confocal configuration; see Figure S4. The monochromatic light filtered from a supercontinuum laser (SuperK FIANIUM) is collimated by a lens to illuminate the sample. The transmitted pattern is imaged by an objective lens (20×, 0.4 NA, ZEISS) and recorded by a charge-couple-device camera (WITec). Figure 3e displays the captured images (raw data) of our sample at the illuminating wavelengths from 500 to 700 nm with an interval of 10 nm. The "pistol" pattern is distinguishable at the wavelengths from 500 to 530 nm, where the strong absorption dominates optical responses. However, this "pistol" disappears within the range from 540 to 700 nm, yielding an experimental bandwidth of 160 nm for our masquerade.

The measured transmission spectra through the film (*i.e.*, the "pistol" area) and metastructures is another approach to evaluate the masquerade. A weakly focused beam with a diameter of ~10 μm is used to illuminate three parts of sample: the "pistol" area, the nanodisk array, and the bare quartz, leaving the transmitted intensity labeled as I_{obj}, I_{MS}, and I_{ref}, respectively. Thus, the experimental transmission spectra are calculated as $T_{obj} = I_{obj}/I_{ref}$ for the object "pistol" and $T_{MS} = I_{MS}/I_{ref}$ for the metastructures. In Figure 3f, both measured spectra have a similar distribution over the spectrum from 500 to 700 nm, resulting in the tiny difference of <3% that cannot be distinguished clearly. Therefore, the relative difference defined as $\Delta_T = |T_{obj} - T_{MS}|/[(T_{obj} + T_{MS})/2]$ is employed here. A small Δ_T means that the "pistol" is invisible, indicating a good camouflage. Derived from the experimental spectra, the Δ_T in Figure 3g shows that the relative difference Δ_T is large at the shorter wavelengths, which coincides well with the observed pictures in Figure 3a.

Broadband Masquerade. The well-behaved masquerade at the wavelengths from 540 to 700 nm suggests the potential camouflage under the broadband illumination. Experimentally, a supercontinuum laser (SuperK Fianium) is used as the illuminating source. Note that a color CCD (WITec) can usually capture light at the wavelengths from 400 to 700 nm, which covers the spectrum of the proposed masquerade. In Figure 1c, the recorded image exhibits only a "cat" pattern,

https://dx.doi.org/10.1021/acsnano.0c03401
ACS Nano 2020, 14, 7529−7537

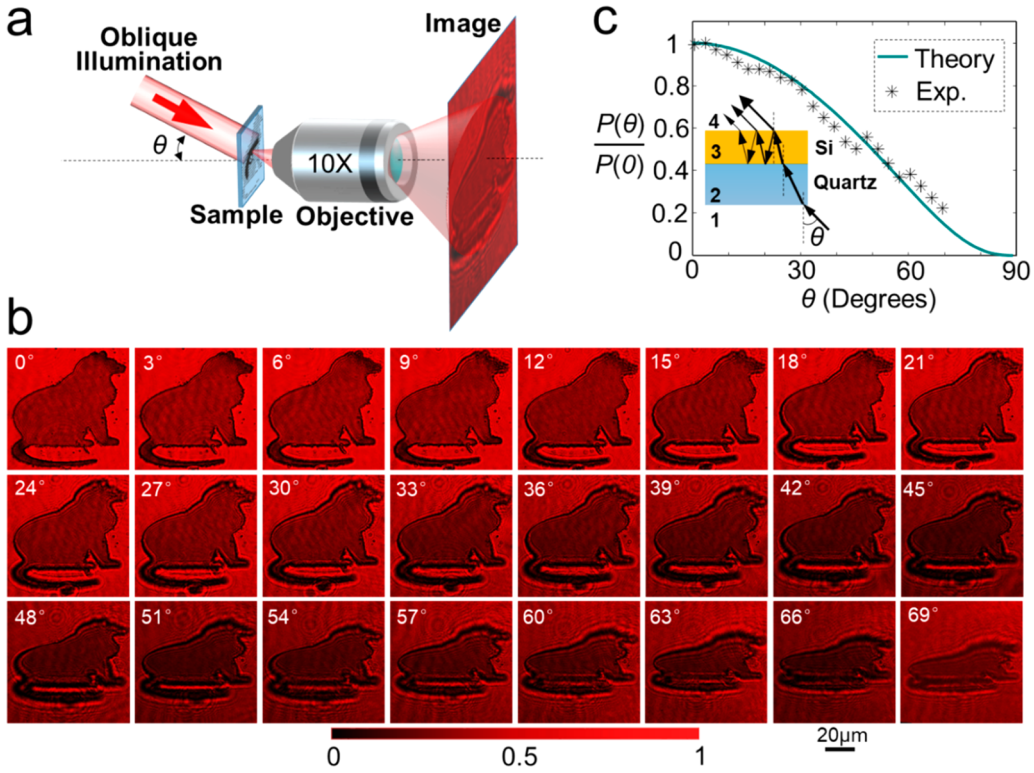

Figure 5. Characterization of multiple view angles. (a) Sketch for measuring the angle-of-view in the experiment by using an oblique illumination and keeping the other components fixed. (b) Experimental images under the oblique illumination with an angle θ from 0° to 69°. (c) Simulated (solid) and experimental (asterisk) power recorded by a CCD camera. The simulated value is calculated by the transmission of light through a Si film of 305 nm thickness, as sketched in the inset.

implying that the object "pistol" is camouflaged perfectly. The feature of ~160 nm bandwidth confirms that the photonic masquerade is superior to optical cloaking that usually operates at a single wavelength.

Phase Measurement. To unveil the phase difference between the metastructure and object, a modified Mach–Zehnder interferometer (Figure 4a) is employed experimentally to map the transmitted phase of the sample (see Methods). At the exemplified wavelength of 633 nm, the interfered pattern between the optical signal from our sample and a quasi-collimated Gaussian beam is recorded by the camera and displayed in Figure 4b. The interfered fringes within the "cat" shape have no dislocation, implying no significant phase difference. To quantify the phase in the "cat" pattern, a phase retrieval algorithm based on fast Fourier transformation[43] (see Methods) is used, thereby creating the retrieved amplitude (Figure 4c) and phase (Figure 4d) profiles that have no jump at the interface between the "pistol" and the surrounding metastructures. To exhibit the details, a line-scanning phase profile (along the white-dashed line in Figure 4d) across the object, the metastructures, and their substrate is shown in Figure 4e. It denotes that the phase difference between the object and the metastructure is smaller than 0.1π, which agrees well with our simulation (see the case h = 15 nm in Figure 2e). Therefore, both the object and metastructures cannot be discriminated, which provides the proof of phase for the proposed masquerade.

Although the metastructure and the "pistol" object are different in the geometry and appearance, both parts show the identical performance, which allows us to analyze the phase difference (Δ_{phase}) between the entire "cat" and the substrate. In Figure 4f, the simulated Δ_{phase} is calculated by using the FDTD method, while the experimental data is extracted from the retrieved phase at the wavelengths of 633 nm (Figure 4e) and 593 and 532 nm (Figure S5). The retrieved Δ_{phase} is added by a wrapped phase of $2n\pi$ (n is an integer), without any influence on its original value due to the sinusoidal oscillation of a monochromatic light. The good agreement between simulation and experiment indicates that the "cat" pattern has a highly consistent phase delay over a wide spectrum.

Multiple Angles-of-View. To measure its angle-of-view, we carry out the experiment by illuminating the sample with an oblique plane wave at the exemplified wavelength of 633 nm (Figure 5a). The recorded images by the color CCD are shown in Figure 5 by addressing the tilting angle θ from 0° to 69° with an interval of 3°. The "pistol" pattern is not observed at the different angles, implying a good masquerade with an angle-of-view of 2 × 69°. The tilting angle θ could be larger in theory, but it is experimentally limited by low transmission under the large θ illumination and finite field-of-view of the collection objective. Therefore, each captured image in Figure 5b is normalized to its own maximum intensity, hereby revealing the details for a better observation.

Figure 5c shows the transmitted power (normalized to the power at the case of normal incidence) through the entire "cat" pattern under the oblique illumination. Since both the object film and the metastructure behave identically, the transmission of a 305 nm-thick Si film on the quartz substrate (see the inset in Figure 5c) is employed as the theoretical prediction (see Methods). The experimental data are extracted directly from the recorded images by using the total power encircled within a square area (*e.g.*, ~14 μm × 14 μm) of the "cat" pattern. Both

https://dx.doi.org/10.1021/acsnano.0c03401
ACS Nano 2020, 14, 7529–7537

experimental and simulated results coincide well, showing the monotonously decreasing tendency in the transmission with the increment of the illuminating angle θ. It confirms that the proposed masquerade is systematically robust over large-angle illumination.

Although the 305 nm-thickness film is used here for an example, the proposed masquerade is also valid for the film with different thicknesses. Figure S6 shows the simulated transmission of the metastructure for the thickness L varying from 200 to 500 nm, indicating nearly the same h_{max} of 15 nm. This result has 2-fold significance. First, it implies that optical masquerade has good universality without the rigorous limitation on the thickness of the camouflaged object. Second, the constant h_{max} for Si film unveils that the excited nanomodes resonate locally (*e.g.*, the middle inset for the case h = 150 nm in Figure 2c), without the dependence on the thickness L of the film. Thus, once the local cavity is formed, the nanomodes begin to oscillate, accompanied with the electromagnetic radiation that leads to a drop of transmission because of its destructive interference with the background. Since the material and diameter of the nanodisks are given in the metastructure, it yields a local cavity with a nearly identical h_{max}. Note that the second issue cannot be predicted by using the perturbation theory because eq 3 is obtained under the assumption of a homogeneous medium where no local cavity is considered.

In addition, the parameter h_{max} will change if a material with a different refractive index is employed. For example, when the silicon used here is substituted by the lower-index materials such as titanium dioxide (TiO_2)[44] or silicon nitride (Si_3N_4),[45] the simulated h_{max} increases, as shown in Figure S7. For a low-index material, the volumes of the nanomodes increase due to the increment of the effective wavelength (λ_0/n, where λ_0 is the wavelength in vacuum and n is the refractive index) in the metastructure, resulting in the increased h_{max}. Therefore, the proposed masquerade can be extended to other material platforms.

As a camouflage, the optical masquerade has four distinct features. First, it enables a large angle-of-view observation and broadband operation at visible frequencies simultaneously, which is challenging for optical cloaking. Second, our strategy does not destroy the objects because there is no spatial overlapping between the objects and the metastructures, facilitating the fabrication of the metastructures by using the matured top-town lithography. Third, the optical masquerade releases the dependence on the environmental variation, thus offering a low-cost camouflage. Finally, the shape and size of the camouflaged object are not limited in principle because the small-pixel-pitch metastructures enable a flexible arrangement with high precision. Although we just demonstrate a simple object that has the fixed response over the amplitude and phase of monochromatic light, the complicated objects (*e.g.*, black–white zebra) can also be camouflaged by introducing nanostructures with different geometries. Moreover, the proposed masquerade could also work in a reflective mode, where a thick metal layer (such as Au, Ag, Al, *etc.*) between the metasurfaces and substrate is required to increase the reflection of light (see Figure S8).

CONCLUSION

In summary, we have demonstrated an optical masquerade with perturbative metasurfaces that can camouflage an object into another irrelative one by mimicking the optical properties of the object with the carefully designed nanodisks. Our results verify its robustness to broadband operation, large-angle oblique illumination, different materials, and the geometry of objects. By suppressing the resonances of the nanomodes, we show a counterintuitive method to develop metasurfaces for the application of camouflage, which might benefit optical security, anticounterfeiting, information encoding, and military usage.

METHODS

Fabrication. E-beam lithography (EBL, ELS-7000, Elionix) was used to pattern the nanodisk shape into hydrogen silsesquioxane (HSQ) resist with a thickness of ~80 nm. After that, the HSQ resist is developed with a NaOH/NaCl solution for 1 min and then washed by DI water, acetone, and IPA, followed by being blown dry with a nitrogen gas flow.[46] To fabricate the proposed metastructure with an etching height of h = 15 nm, the exposure dosage of EBL is optimized so that the resist at the gap between the nanodisks is also exposed due to the backward scattering of the accelerated electrons. When the dosage is tuned precisely, the resist at the nanodisks region can be fully exposed while the resist at the gap between the nanodisks (*i.e.*, the adjacent area located among the four nanodisks) is partially exposed. Thus, after the resist development, we can get a three-dimensional HSQ pattern (see Figure 3b,c). Within the patterning area, the resist at the nanodisk region is high and the resist at the gap region is low; however, there is no resist outside the patterning area. Then, a dry etching of Si is followed with the controlled time. Thus, the Si at the nanodisk region is not etched, and the Si at the gap region is partially etched, leaving the required height of h. To find the right exposure dosage of EBL, we patterned an array of the same sample with the small-step interval of dosage; see Figure S3. It shows that the larger dosage of EBL leads to shallower HSQ nanodisks. It is because the HSQ in the gap region (between nanodisks) is experiencing a higher dosage, due to the stronger backscattered secondary electrons. Consequently, after the salty development, the nanogaps will be slowly filled up, with respect to the increased exposure dosage. In other words, when the exposure dosage is increased, the relative height between the HSQ nanodisk and the gap region is getting smaller. Therefore, due to the protection of overexposed HSQ in the gap region, the thickness of the final etched Si nanodisks will become thinner for a larger EBL dosage.

Note that when the EBL dwell time is fixed at an identical sample, the effective dose locally of the backscattered electrons is mainly determined by the density of patterns. The dense pattern will lead to stronger backscattering of secondary electrons, hereby creating a nonuniform thickness of the nanodisk array (see Figure 3b,c). To solve the problem, we suggest two methods. First, for the overdosage case used in this work, a position-dependent EBL dosage is needed by taking into account the detailed shape of the nanostructures. It needs plenty of customized programming for most EBL machines. The other method is to use a normal dosage (without any overexposure and backscattering of electrons) and expose only HSQ at the nanodisk region. After the development, only HSQ nanodisks are kept on the top of the silicon film. Then, a dry etching of Si is followed with carefully controlled rates and time of etching, which is the key of the second method due to the extremely small etching thickness of 15 nm.

Experimental Setup for Phase Measurement. A modified Mach–Zehnder interferometer is used to measure the phase response of the fabricated device. In Figure 4a, a high-coherence laser with linear polarization is expanded by a telescopic system compose of two lenses (L_1 and L_2), where a pinhole (PH) of 20 μm is located at their confocal plane in order to obtain a quasi-Gaussian beam. A half-wave plate (HWP_1) is then used to tune the power of reference and signal beams that are separated by a polarization-sensitive beam splitter (PBS), hereby facilitating a high-contrast inference pattern. The signal beam is weakly focused by lens L_3 onto the full device, so as to increase the transmitted power through the sample (containing the pistol object and the metastructures). Their combined "cat" pattern is

https://dx.doi.org/10.1021/acsnano.0c03401
ACS Nano 2020, 14, 7529–7537

imaged by a 10× objective lens onto a color camera. The reference beam is expanded further by another telescopic system (L_4 and L_5) to match the dimension of the magnified "cat" pattern; meanwhile, an additional half-wave plate (HWP_2) is adopted here to keep the identical polarization between the reference and signal beams for high-visibility interfered fringes. Finally, the signal beam carrying the "cat" pattern and the reference beam are combined together by a polarization-independent (50:50) beam splitter, and the interference occurs when both beams have a slightly tilted angle. The interfered patterns are recorded by the color camera.

Phase Retrieval. We retrieve the phase from the interference pattern by using a fast Fourier transform (FFT) that could separate the spectrum (±1 orders) of the signal beam from that (0 order) of the reference beam. Next, only the spectrum of the signal beam is maintained and shifted to the center of the spectrum domain, leading to a new spectrum whose inverse FFT gives the retrieved amplitude and phase of the combined "cat" pattern. A detailed illustration about this phase retrieval process can be found in our previous work.[43]

Optical Transmission through a Si Film. According to the Fresnel formulas,[47] the transmittance at the incident angle θ can be described by $T(\theta) = t_{12}t_{23}t_{34}e^{i\beta}/(1 - r_{34}r_{32}e^{i\beta})$, where t_{ij} and r_{ij} are the transmittance and reflectivity of light from medium i to medium j and the parameter $\beta = 2k_3L$ (where $k_3 = 2\pi n_3/\lambda_0$ and $L = d/\cos\theta_3$ are the wavenumber and the single-trip traveling distance in the Si film and n_3, θ_3, and d are the refractive index, the refractive angle, and the thickness of the Si film, respectively). Considering that the normal direction of the detector has the angle θ with the incident light (see Figure 5a), the recorded power (normalized to the incident power) by the detector can be theoretically expressed as $P(\theta) = |T(\theta)|^2 \times \cos\theta$. It gives the theoretical prediction denoted by the solid curve of $P(\theta)/P(0)$ at $\lambda_0 = 633$ nm in Figure 5c.

ASSOCIATED CONTENT

Supporting Information

The Supporting Information is available free of charge at https://pubs.acs.org/doi/10.1021/acsnano.0c03401.

Experimentally measured refraction index of a 305 nm-thick Si film on the quartz substrate by using an ellipsometer; simulated electric fields in metastructures and Si film at three typical wavelengths of 500, 600, and 700 nm; AFM images of photoresist (HSQ) after development; experimental setup for characterizing the optical masquerade; experimental interference patterns, the retrieved phase, and their line-scanning profiles; simulated transmission of the metastructures with different thicknesses; simulated transmission of the metastructures with different materials; proposed photonic masquerade in reflection mode (PDF)

AUTHOR INFORMATION

Corresponding Authors

Kun Huang − *Department of Optics and Optical Engineering, University of Science and Technology of China, Hefei, Anhui 230026, China; Institute of Materials Research and Engineering, Agency for Science, Technology and Research (A*STAR), Singapore 138634 Singapore;* orcid.org/0000-0002-9391-149X; Email: huangk17@ustc.edu.cn

Zhaogang Dong − *Institute of Materials Research and Engineering, Agency for Science, Technology and Research (A*STAR), Singapore 138634 Singapore;* orcid.org/0000-0002-0929-7723; Email: dongz@imre.a-star.edu.sg

Authors

Dong Zhao − *Department of Optics and Optical Engineering, University of Science and Technology of China, Hefei, Anhui 230026, China*

Febiana Tjiptoharsono − *Institute of Materials Research and Engineering, Agency for Science, Technology and Research (A*STAR), Singapore 138634 Singapore*

Yunjie Chen − *Institute of Materials Research and Engineering, Agency for Science, Technology and Research (A*STAR), Singapore 138634 Singapore*

Calvin Pei Yu Wong − *Institute of Materials Research and Engineering, Agency for Science, Technology and Research (A*STAR), Singapore 138634 Singapore;* orcid.org/0000-0002-3135-7534

Xiaosong Tang − *Institute of Materials Research and Engineering, Agency for Science, Technology and Research (A*STAR), Singapore 138634 Singapore*

Joel K. W. Yang − *Institute of Materials Research and Engineering, Agency for Science, Technology and Research (A*STAR), Singapore 138634 Singapore; Singapore University of Technology and Design, Singapore 487372 Singapore;* orcid.org/0000-0003-3301-1040

Complete contact information is available at: https://pubs.acs.org/10.1021/acsnano.0c03401

Author Contributions

K.H. conceived the idea, carried out the numerical simulations, built up the optical measuring systems, and characterized the samples. Z.D. and J.K.W.Y. prepared and fabricated the samples. F.T. and Z.D. did the dry etching of the sample. F.T. and Z.D. did the dry etching of the sample. Y.C., C.P.Y.W., and F.T. did the atomic force microscopy measurements and interpretations. D.Z. took the SEM images of the samples. X.T. did the hydrofluoric (HF) acid treatment of early batch samples. K.H., Z.D., and J.K.W.Y. wrote the manuscript and discussed the results. K.H. supervised the overall project. All the authors analyzed the data.

Notes

The authors declare no competing financial interest.

ACKNOWLEDGMENTS

K.H. thanks Prof. Fangwen Sun and Dr. Xiangdong Chen for providing the experimental equipment and Prof. Yefeng Yu for his valuable suggestions. K.H. thanks the National Natural Science Foundation of China (Grant Nos. 61875181 and 61705085), USTC Research Funds of the Double First-Class Initiative (Grant No. YD2030002003), "the Fundamental Research Funds for the Central Universities" in China, and the CAS Pioneer Hundred Talents Program and is grateful for the support from the University of Science and Technology of China's Centre for Micro and Nanoscale Research and Fabrication. In addition, Z.D. and J.K.W.Y. acknowledge the funding support of A*STAR-JCO under the project number 1437C00135 and the A*STAR SERC Pharos project (Grant 1527300025).

REFERENCES

(1) Stevens, M.; Merilaita, S. *Animal Camouflage: Mechanisms and Function*; Cambridge University Press: New York, 2011.

(2) Morin, S. A.; Shepherd, R. F.; Kwok, S. W.; Stokes, A. A.; Nemiroski, A.; Whitesides, G. M. Camouflage and Display for Soft Machines. *Science* **2012**, *337*, 828−832.

(3) Pendry, J. B.; Schurig, D.; Smith, D. R. Controlling Electromagnetic Fields. *Science* **2006**, *312*, 1780−1782.

(4) Han, T.; Bai, X.; Gao, D.; Thong, J. T.; Li, B.; Qiu, C.-W. Experimental Demonstration of a Bilayer Thermal Cloak. *Phys. Rev. Lett.* **2014**, *112*, 054302.

(5) Xu, H.; Shi, X.; Gao, F.; Sun, H.; Zhang, B. Ultrathin Three-Dimensional Thermal Cloak. *Phys. Rev. Lett.* **2014**, *112*, 054301.
(6) Liu, R.; Ji, C.; Mock, J.; Chin, J.; Cui, T.; Smith, D. Broadband Ground-Plane Cloak. *Science* **2009**, *323*, 366−369.
(7) Smith, D. R.; Padilla, W. J.; Vier, D. C.; Nemat-Nasser, S. C.; Schultz, S. Composite Medium with Simultaneously Negative Permeability and Permittivity. *Phys. Rev. Lett.* **2000**, *84*, 4184−4187.
(8) Xie, X.; Li, X.; Pu, M.; Ma, X.; Liu, K.; Guo, Y.; Luo, X. Plasmonic Metasurfaces for Simultaneous Thermal Infrared Invisibility and Holographic Illusion. *Adv. Funct. Mater.* **2018**, *28*, 1706673.
(9) Ergin, T.; Stenger, N.; Brenner, P.; Pendry, J. B.; Wegener, M. Three-Dimensional Invisibility Cloak at Optical Wavelengths. *Science* **2010**, *328*, 337−339.
(10) Chen, H.; Chan, C. T.; Sheng, P. Transformation Optics and Metamaterials. *Nat. Mater.* **2010**, *9*, 387−396.
(11) Liu, Y.; Zhang, X. Metamaterials: A New Frontier of Science and Technology. *Chem. Soc. Rev.* **2011**, *40*, 2494−2507.
(12) Valentine, J.; Li, J.; Zentgraf, T.; Bartal, G.; Zhang, X. An Optical Cloak Made of Dielectrics. *Nat. Mater.* **2009**, *8*, 568−571.
(13) Kundtz, N.; Smith, D. R. Extreme-Angle Broadband Metamaterial Lens. *Nat. Mater.* **2010**, *9*, 129−132.
(14) Zheng, B.; Zhu, R.; Jing, L.; Yang, Y.; Shen, L.; Wang, H.; Wang, Z.; Zhang, X.; Liu, X.; Li, E.; et al. 3D Visible-Light Invisibility Cloak. *Adv. Sci.* **2018**, *5*, 1800056.
(15) Yang, J.; Huang, C.; Wu, X.; Sun, B.; Luo, X. Dual-Wavelength Carpet Cloak Using Ultrathin Metasurface. *Adv. Opt. Mater.* **2018**, *6*, 1800073.
(16) Deng, Y.; Xu, S.; Zhang, R.; Zheng, B.; Chen, H.; Gao, F.; Yu, F.; Zhang, B.; Chen, H. Ultra-Broadband Carpet Cloak for Transverse-Electric Polarization. *J. Opt.* **2016**, *18*, 044006.
(17) Chen, X.; Luo, Y.; Zhang, J.; Jiang, K.; Pendry, J. B.; Zhang, S. Macroscopic Invisibility Cloaking of Visible Light. *Nat. Commun.* **2011**, *2*, 176.
(18) Zhang, B.; Luo, Y.; Liu, X.; Barbastathis, G. Macroscopic Invisibility Cloak for Visible Light. *Phys. Rev. Lett.* **2011**, *106*, 033901.
(19) Gabrielli, L. H.; Cardenas, J.; Poitras, C. B.; Lipson, M. Silicon Nanostructure Cloak Operating at Optical Frequencies. *Nat. Photonics* **2009**, *3*, 461−463.
(20) Skelhorn, J.; Rowland, H. M.; Speed, M. P.; Ruxton, G. D. Masquerade: Camouflage without Crypsis. *Science* **2010**, *327*, 51−51.
(21) Lalanne, P.; Astilean, S.; Chavel, P.; Cambril, E.; Launois, H. Blazed Binary Subwavelength Gratings with Efficiencies Larger than Those of Conventional Echelette Gratings. *Opt. Lett.* **1998**, *23*, 1081−1083.
(22) Bomzon, Z.; Kleiner, V.; Hasman, E. Pancharatnam-Berry Phase in Space-Variant Polarization-State Manipulations with Subwavelength Gratings. *Opt. Lett.* **2001**, *26*, 1424−1426.
(23) Yu, N.; Genevet, P.; Kats, M. A.; Aieta, F.; Tetienne, J.-P.; Capasso, F.; Gaburro, Z. Light Propagation with Phase Discontinuities: Generalized Laws of Reflection and Refraction. *Science* **2011**, *334*, 333−337.
(24) Yu, N.; Capasso, F. Flat Optics with Designer Metasurfaces. *Nat. Mater.* **2014**, *13*, 139−150.
(25) Genevet, P.; Capasso, F. Holographic Optical Metasurfaces: A Review of Current Progress. *Rep. Prog. Phys.* **2015**, *78*, 024401.
(26) Zhang, L.; Mei, S.; Huang, K.; Qiu, C.-W. Advances in Full Control of Electromagnetic Waves with Metasurfaces. *Adv. Opt. Mater.* **2016**, *4*, 818−833.
(27) Glybovski, S. B.; Tretyakov, S. A.; Belov, P. A.; Kivshar, Y. S.; Simovski, C. R. Metasurfaces: From Microwaves to Visible. *Phys. Rep.* **2016**, *634*, 1−72.
(28) Ding, F.; Pors, A.; Bozhevolnyi, S. I. Gradient Metasurfaces: A Review of Fundamentals and Applications. *Rep. Prog. Phys.* **2018**, *81*, 026401.
(29) Chen, H.-T.; Taylor, A. J.; Yu, N. A Review of Metasurfaces: Physics and Applications. *Rep. Prog. Phys.* **2016**, *79*, 076401.
(30) Huang, K.; Liu, H.; Garcia-Vidal, F. J.; Hong, M.; Luk'yanchuk, B.; Teng, J.; Qiu, C.-W. Ultrahigh-Capacity Non-Periodic Photon Sieves Operating in Visible Light. *Nat. Commun.* **2015**, *6*, 7059.
(31) Luo, X. Principles of Electromagnetic Waves in Metasurfaces. *Sci. China: Phys., Mech. Astron.* **2015**, *58*, 594201.
(32) Huang, Y.; Luo, J.; Pu, M.; Guo, Y.; Zhao, Z.; Ma, X.; Li, X.; Luo, X. Catenary Electromagnetics for Ultra-Broadband Lightweight Absorbers and Large-Scale Flat Antennas. *Adv. Sci.* **2019**, *6*, 1801691.
(33) Huo, P.; Zhang, C.; Zhu, W.; Liu, M.; Zhang, S.; Zhang, S.; Chen, L.; Lezec, H. J.; Agrawal, A.; Lu, Y.; Xu, T. Photonic Spin-Multiplexing Metasurface for Switchable Spiral Phase Contrast Imaging. *Nano Lett.* **2020**, *20*, 2791−2798.
(34) Huang, K.; Dong, Z.; Mei, S.; Zhang, L.; Liu, Y.; Liu, H.; Zhu, H.; Teng, J.; Luk'yanchuk, B.; Yang, J. K.; Qiu, C. Silicon Multi-Meta-Holograms for the Broadband Visible Light. *Laser Photonics Rev.* **2016**, *10*, 500−509.
(35) Huang, K.; Deng, J.; Leong, H. S.; Yap, S. L. K.; Yang, R. B.; Teng, J.; Liu, H. Ultraviolet Metasurfaces of ≻80% Efficiency with Antiferromagnetic Resonances for Optical Vectorial Anti-Counterfeiting. *Laser Photonics Rev.* **2019**, *13*, 1800289.
(36) Dong, Z.; Ho, J.; Yu, Y. F.; Fu, Y. H.; Paniagua-Dominguez, R.; Wang, S.; Kuznetsov, A. I.; Yang, J. K. Printing beyond SRGB Color Gamut by Mimicking Silicon Nanostructures in Free-Space. *Nano Lett.* **2017**, *17*, 7620−7628.
(37) Dong, Z.; Wang, T.; Chi, X.; Ho, J.; Tserkezis, C.; Yap, S. L. K.; Rusydi, A.; Tjiptoharsono, F.; Thian, D.; Mortensen, N. A.; et al. Ultraviolet Interband Plasmonics with Si Nanostructures. *Nano Lett.* **2019**, *19*, 8040−8048.
(38) Huang, K.; Liu, H.; Si, G.; Wang, Q.; Lin, J.; Teng, J. Photon-Nanosieve for Ultrabroadband and Large-Angle-of-View Holograms. *Laser Photonics Rev.* **2017**, *11*, 1700025.
(39) Jackson, J. D. *Classical Electrodynamics*; Wiley: New York, 1999.
(40) Choy, T. C. *Effective Medium Theory: Principles and Applications*; Oxford University Press: Oxford, 2015.
(41) Luk'yanchuk, B.; Zheludev, N. I.; Maier, S. A.; Halas, N. J.; Nordlander, P.; Giessen, H.; Chong, C. T. The Fano Resonance in Plasmonic Nanostructures and Metamaterials. *Nat. Mater.* **2010**, *9*, 707−715.
(42) Joe, Y. S.; Satanin, A. M.; Kim, C. S. Classical Analogy of Fano Resonances. *Phys. Scr.* **2006**, *74*, 259−266.
(43) Huang, K.; Liu, H.; Restuccia, S.; Mehmood, M. Q.; Mei, S.; Giovannini, D.; Danner, A.; Padgett, M. J.; Teng, J.; Qiu, C.-W. Spiniform Phase-Encoded Metagratings Entangling Arbitrary Rational-Order Orbital Angular Momentum. *Light: Sci. Appl.* **2018**, *7*, 17156.
(44) DeVore, J. R. Refractive Indices of Rutile and Sphalerite. *J. Opt. Soc. Am.* **1951**, *41*, 416−419.
(45) Luke, K.; Okawachi, Y.; Lamont, M. R.; Gaeta, A. L.; Lipson, M. Broadband Mid-Infrared Frequency Comb Generation in a Si_3n_4 Microresonator. *Opt. Lett.* **2015**, *40*, 4823−4826.
(46) Dong, Z.; Asbahi, M.; Lin, J.; Zhu, D.; Wang, Y. M.; Hippalgaonkar, K.; Chu, H.-S.; Goh, W. P.; Wang, F.; Huang, Z.; Yang, J. K. W. Second-Harmonic Generation from Sub-5 Nm Gaps by Directed Self-Assembly of Nanoparticles onto Template-Stripped Gold Substrates. *Nano Lett.* **2015**, *15*, 5976−5981.
(47) Born, M.; Wolf, E. *Principles of Optics: Electromagnetic Theory of Propagation, Interference and Diffraction of Light*; Cambridge Univ. Press: Cambridge, 1999.

https://dx.doi.org/10.1021/acsnano.0c03401
ACS Nano 2020, 14, 7529−7537